ADVANCED ENERGY MATERIALS

www.advenergymat.de

Phase Transformation and Microstructural Evolution of CuS Electrodes in Solid-State Batteries Probed by In Situ 3D X-Ray Tomography

Zhenggang Zhang, Kang Dong, Katherine A. Mazzio, André Hilger, Henning Markötter, Fabian Wilde, Tobias Heinemann, Ingo Manke, and Philipp Adelhelm**

Copper sulfide shows some unique physico-chemical properties that make it appealing as a cathode active material (CAM) for solid-state batteries (SSBs). The most peculiar feature of the electrode reaction is the reversible formation of μm-sized Cu crystals during cycling, despite its large theoretical volume change (75%). Here, the dynamic microstructural evolution of CuS cathodes in SSBs is studied using in situ synchrotron X-ray tomography. The formation of μm-sized Cu within the CAM particles can be clearly followed. This process is accompanied by crack formation that can be prevented by increasing the stack pressure from 26 to 40 MPa. Both the Cu inclusions and cracks show a preferential orientation perpendicular to the cell stack pressure, which can be a result of a z-oriented expansion of the CAM particles during lithiation. In addition, cycling leads to a z-oriented reversible displacement of the cathode pellet, which is linked to the plating/stripping of the Li counter electrode. The pronounced structural changes cause pressure changes of up to 6 MPa within the cell, as determined by operando stack pressure measurements. Reasons for the reversibility of the electrode reaction are discussed and are attributed to the favorable combination of soft materials.

1. Introduction

Solid-state batteries (SSBs) are one of the most promising technologies under development toward batteries with higher energy density and improved safety.[1] Compared to conventional lithium-ion batteries (LIBs) that are based on solid electrodes with liquid electrolytes, solid-state batteries consist only of solids, a fact that is often emphasized by calling them all-solid-state batteries (ASSBs). In the following, we use the abbreviation SSBs.

Due to their solid nature, the performance of SSBs strongly depends on how well the physical contact between the active materials (AMs, anode, cathode) and the solid electrolytes (SEs) are preserved during battery operation.[2] Electrodes and cells are therefore assembled and cycled at elevated pressures.[3,4] Fabrication pressures and stack pressures are typically in the range of 50–370 and 5–70 MPa, respectively.[5,6] However, maintaining good contact between the materials remains an issue because the shuttling of lithium-ions between the electrodes during cycling can lead to electrode material volume changes that can easily lead to crack formation and/or particle contact loss.[7] Such failure mechanisms can be observed by scanning electron microscopy (SEM) or focused ion beam scanning electron microscopy (FIB-SEM), although a limitation of these types of measurements is that they are done post-mortem, i.e., the cells must be disassembled and studied without the pressure that is applied during battery cycling.[4,8]

A powerful alternative is X-ray tomography (XRT), which enables complete cells or electrodes to be analyzed under operating conditions.[9] The technique has recently been used to study several symmetric Li|SE|Li cells and SSBs with various electrode materials.[10,11] Through these studies, the Li/SE interphase evolution[11,12] and SE cracking and short-circuiting[10,13,14] in SSBs have been visualized. The majority of studies have employed layered oxides (NCM, NCA) as cathode active materials (CAMs).[15] Despite the relatively small volume changes of these materials during cycling (for example, NCM811 has a volume change of 7.8 ± 1.5 vol% when the capacity reaches 189 mAh g^{-1}), contact loss was clearly observed and linked to

Z. Zhang, K. A. Mazzio, T. Heinemann, P. Adelhelm
Institut für Chemie
Humboldt Universität zu Berlin
Brook-Taylor-Str. 2, 12489 Berlin, Germany
E-mail: philipp.adelhelm@hu-berlin.de

K. Dong, K. A. Mazzio, A. Hilger, H. Markötter, I. Manke, P. Adelhelm
Helmholtz-Zentrum Berlin für Materialien und Energie
Hahn-Meitner-Platz 1, 14109 Berlin, Germany
E-mail: kang.dong@helmholtz-berlin.de

H. Markötter
Bundesanstalt für Materialforschung und -Prüfung
Unter den Eichen, 87, 12205 Berlin, Germany

F. Wilde
Helmholtz-Zentrum Hereon
Max-Planck Strasse 1, 21502 Geesthacht, Germany

The ORCID identification number(s) for the author(s) of this article can be found under https://doi.org/10.1002/aenm.202203143.

DOI: 10.1002/aenm.202203143

cell degradation.[2,16] Relevant aspects of designing the structure of cathodes for SSBs have recently been discussed by Minnmann et al.[17]

In search of alternative CAMs, copper sulfide has been recently studied in SSBs. Copper sulfides are naturally occurring minerals and show specific properties that make them appealing for SSBs.[18] An advantage of CuS compared to layered oxides is its high theoretical capacity of 561 mAh g^{-1}. On the other hand, the high capacity leads to a volume expansion as large as 75%. The idealized cell reaction can be formulated as $2Li + CuS = Cu + Li_2S$ ($E = 1.96$ V). The energy density of this reaction equals 961 Wh kg^{-1} which, despite the lower voltage, is greater than that of layered oxides as CAMs.

Reactions of this type are typically classified as conversion reactions. A common observation for conversion reactions is that lithiation of the active material leads to the formation of nanostructures.[19,20] In the case of CuS, one would expect the formation of copper nanoparticles in an amorphous Li_2S matrix. In contrast to this expectation, Debart et al. showed that for cells with liquid electrolyte, CuS behaves differently and large Cu crystals form during battery discharge, i.e., a displacement reaction takes place.[21] This behavior was attributed to a favorable lattice match between the different phases. The reaction was believed to be poorly reversible, but it turned out that the choice of electrolyte had a strong influence on the cycle life.[22] The formation of large Cu-crystals during lithiation of CuS (that are even visible by eye) was recently also confirmed for SSBs by Santhosha et al.[18] In view of the large volume changes and the phase transformations during cycling, the reversibility of the reaction appears very surprising at first. Next to the favorable lattice match, the high conductivity of Cu^+ and e^- (870 S cm^{-1}) in CuS, combined with its favorable ductility (Mohs hardness of 1–1.5) seem to be relevant factors for affording rechargeability in SSBs. The high conductivity of CuS has allowed the preparation of electrodes without carbon conductive additive, for example.[18] Besides the use of CuS as a CAM in SSBs, the reaction appears to also be an ideal case study for X-ray tomography study thanks to the strong differences in X-ray attenuation between Cu (and Cu-rich phases), the discharge product (Li_2S), and the solid electrolyte (β-Li_3PS_4 in this study).

Here, we study the structural evolution of the reaction between Li and CuS in an SSB under in situ conditions. To allow sufficient transmission of the X-rays, the housing of the SSBs was optimized and the CuS loading was reduced to 8 wt% (see the Experimental Section). Measurements were performed at several states of charge (SOC) under applied vertical (z-direction) stack pressures of 26 and 40 MPa. The measurements clearly show the crack evolution and phase transformation during cycling and provide evidence for a preferred orientation of the Cu crystals and crack formation along the x-y plane. The formation of large Cu crystals is seen from FIB-SEM measurements. The findings are supported by a quantitative analysis of the tomography data which also shows the displacement of CAM particles along the *z*-axis (z-oriented displacement) for the first time. Tomography data are also collected for the 50th cycle of the SSBs and crack formation is shown to be preventable by increasing the stack pressure. The structural changes during cycling also lead to a notable change in the stack pressure which is observed through implementing a force sensor. Overall, the tomography data provide information on phase transformations, crack formation/mitigation, and particle displacement of CuS-based electrodes in SSBs.

2. Results

In situ X-ray tomography studies were carried out utilizing a custom-built cell (**Figure 1**a) that comprises a low X-ray attenuating housing made of polyether ether ketone (PEEK) that has good mechanical stability and high resistance against radiation. To ensure sufficient X-ray transmission and maximize the electrochemical performance of the prototypical CuS electrode, we opted for a low active material loading (4.08 mg cm^{-2}) in the cathode. Overall the cathode consisted of a mixture of CuS, β-Li_3PS_4, and Super C65 conductive carbon black (C65) with a mass ratio of 8:87:5. Note that carbon additive was used herein to ensure sufficient electronic conductivity in the cathode pellets, which is not typically employed with high CuS loading due to the relatively high conductivity of CuS.[18] The SSBs were assembled with a Li|β-Li_3PS_4|cathode sandwich structure (Figure S1a, Supporting Information), the details of which are given in the Experimental Section. To track and visualize the microstructural evolution inside the SSBs, in situ tomography measurements were conducted at different SOC during the first cycle and after 50 cycles in order to investigate the cell degradation after long-term operation.

2.1. Phase Transformation of the CAM

A typical galvanostatic voltage curve for CuS-based SSBs at a constant current density of 10 mA g^{-1} is shown in Figure 1b. The solid circles highlight the measurement points at different characteristic SOC. Tomography measurements were performed at open circuit voltage (OCV), during discharging at 1.7 V (D1.7 V), 1.2 V (D1.2 V), and 0.7 V (D0.7 V), and during charging at 2.5 V (C2.5 V) and 3.0 V (C3.0 V). The virtual cross-sectional views showing the phase evolution of a representative CAM particle at different SOC during 1st cycle are shown in Figure 1c. The CAM cross sections have been color-coded based on the X-ray transmission ratio, and from these results it becomes evident that the CAM particle underwent a phase separation during lithiation, followed by a dissolution of the newly generated phase (red colored) during the subsequent delithiation. The obtained initial discharge capacity (507 mAh g^{-1}, Figure S3a, Supporting Information) is comparable with our previous study (498 mAh g^{-1}) that used a dedicated SSB housing,[18] demonstrating the good working condition of the custom-built PEEK cell. At the OCV state, the CAM particle generally presents a high chemical and structural homogeneity across the particle, with some local visible variations that tend to be the result of CuS grains in the particle in addition to grain boundaries/voids at the sub-µm level as inferred from the morphology observed in a particle cross-section (Figure S2, Supporting Information). During

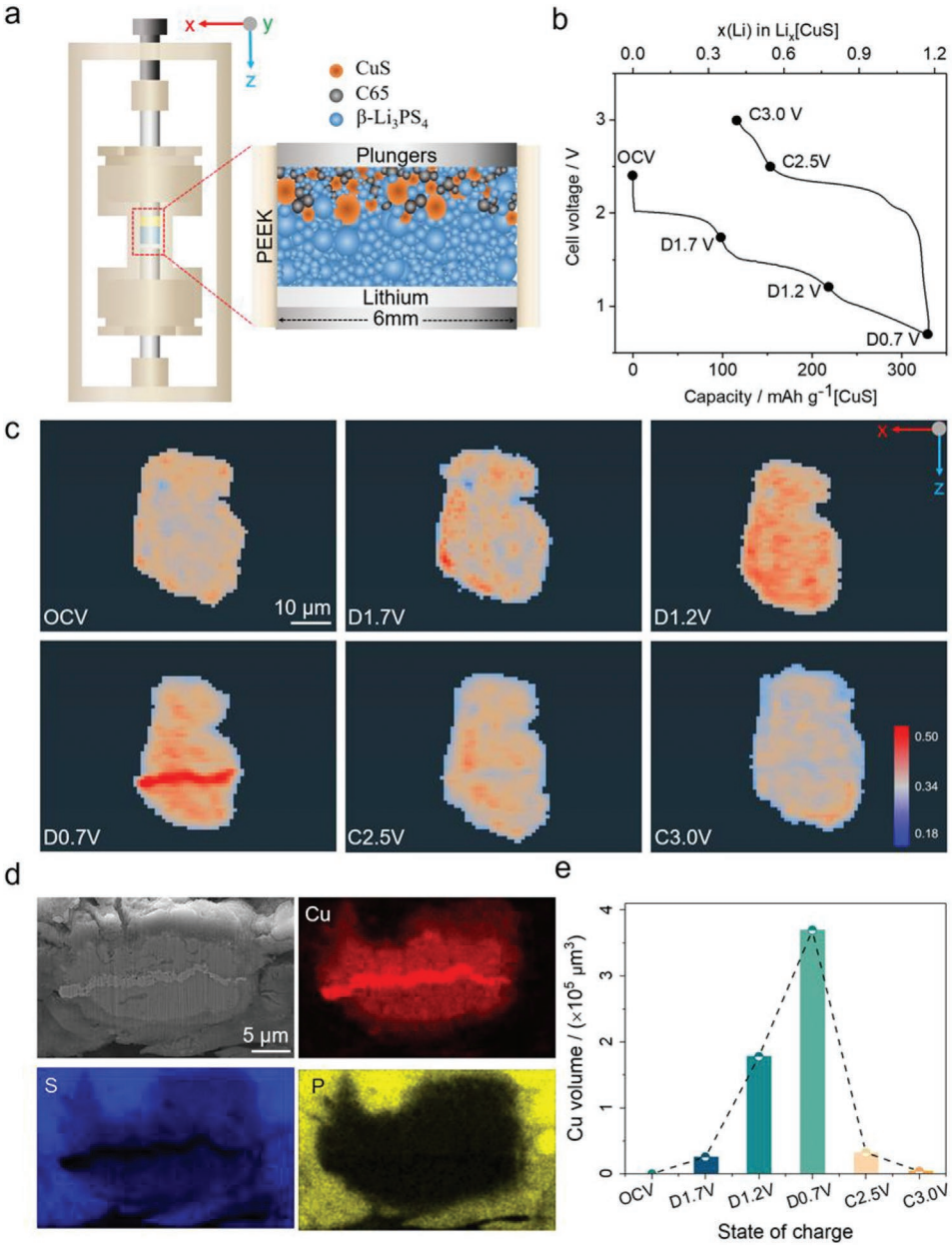

Figure 1. Phase transformation in a CAM particle during lithiation and delithiation. a) A schematic of the SSBs used for in situ 3D tomography measurements. b) The typical galvanostatic discharge–charge curve of a CuS SSB. Tomography measurements were done at different SOC. c) In situ tomography of a SSB with 26 MPa initial stacking pressure. The virtual cross-sectional views of the CAM particle are color-coded based on the local X-ray attenuation (color bar in a.u.), showing the microstructure at different SOC during the first discharge (OCV, 1.7, 1.2, and 0.7 V) and first charge (2.5 and 3.0 V). For ease of visibility, areas with high X-ray attenuation are red, while areas with low attenuation ratios are blue. d) SEM image showing a CuS cathode at the end of discharge after performing FIB cross-sectioning alongside the corresponding EDX mapping of the elemental distribution of Cu (red), sulfur (blue), and phosphorus (yellow). e) Volume quantification of the Cu (high attenuation) material in the electrode during the 1st cycle.

the lithiation of CuS, it is expected that Cu_2S will form as an intermediate phase during the first lithiation plateau, followed by the formation of Cu during the second plateau according to

$$2CuS + 2Li^+ + 2e^- \rightarrow Cu_2S + Li_2S \quad (1)$$

$$Cu_2S + 2Li^+ + 2e^- \rightarrow 2Cu + Li_2S \quad (2)$$

This apparent two-step discharge mechanism is well known,[22] although one has to be aware that the Cu-S phase diagram is more complex, showing several binary compounds with varying homogeneity ranges.[23] The sensitivity of the phases toward pressure has been reported as well.[23] Other off-stoichiometric or metastable intermediate phases may therefore occur during cycling too, although the two-step shape is preserved overall during cycling in SSBs,[18] and is also seen in the in situ SSBs in this study (Figure S3a,b, Supporting

Information). In good agreement with the chemical reaction pathways, areas with slightly higher attenuation (light red) gradually appear locally near the edge of the particle (D1.7 V), and subsequently propagate across the whole particle (D1.2 V). During the last period of the lithiation (D1.2 to D0.7 V), the red color tends to agglomerate, leading to the enrichment of one region and a decrease of the red intensity of the surrounding areas. Thereafter, the consolidated red areas start decaying with the appearance of low attenuation (light blue) regions that spread from the center and border of the particle during delithiation. Such findings are also consistent with the observation of Cu networks after discharge in our previous work.[18] Considering the high mobility of Cu^+ in CuS and Cu_2S,[22,24] this macroscopic phase transformation could be attributed to the fast motion of Cu^+ and agglomeration of Cu within the CuS particle. Through the spatial distribution of the high attenuation zone (coalesced Cu) in the CuS particle (Figure S4, Supporting Information), the preferential orientation of the high attenuation zones can clearly be seen at the state of D0.7 V, i.e., laterally and in parallel with the current collectors (perpendicular to the stack pressure direction). This feature was also observed in other particles throughout the electrode (Figure S3 and Movie S1, Supporting Information).

The phase evolution during cycling was also studied post-mortem by SEM/energy-dispersive X-ray spectroscopy (EDX) measurements. Cross-sectional views before and after lithiation were obtained by FIB milling, as shown in Figure S2 (Supporting Information); and Figure 1d. In line with the tomography results, the uniformly dispersed elements at the pristine state were redistributed with coalescing Cu in the center of the CAM particle with a clear preferential orientation after discharge. The newly-generated phase (white regions) is composed of metallic Cu as unveiled by the nearly invisible sulfur in this region in the EDX images (Figure 1d), and also supported by the high intensity of the Cu signals in the related XRD pattern (Figure S1b, Supporting Information). Overall, the measurements provide clear evidence for the formation of µm-sized Cu with preferred orientation within the parent CAM particle.

Furthermore, the evident absorption contrast between Cu and the other chemical compositions in the SSBs enables us to carry out quantitative analysis of the reaction, in particular for that of the evolving Cu phase (Figure 1e; and Figure S4, Supporting Information). The volume of Cu inclusions within the probed region increases from 0 (OCV, reference value) to 2.56×10^4 µm^3 (D1.7 V), 1.78×10^5 µm^3 (D1.2 V), and finally reaches its apex of 3.7×10^5 µm^3 at D0.7 V. The trend is reversed upon charging and over 90% of the high attenuation volume faded away after reaching 3.0 V. Overall, this clearly supports a reversible phase transformation mechanism.

Regarding the images in Figure 1c, it is worth noting that the particle shows an increase in the fraction of blue areas (low X-ray attenuation) during charging, especially at the location where Cu was formed. At the same time, low X-ray absorption regions corresponding to cracks appear in the electrode as shown by the virtual slices in Figure S3 (Supporting Information). Simultaneously, the attenuation coefficient curves are found to move to lower attenuation coefficient values than that of the OCV state, see Figure S5 (Supporting Information). These features clearly indicate the formation of a more heterogeneous structure, including the formation of voids and cracks.

2.2. Crack Evolution During Cycling

Contact loss and crack formation due to volume variations during cycling is well expected for electrodes in SSBs and has been reported for materials with small (layered oxides,[2,25] 2–7%) and large (S,[26] 80%; Sn,[27] 260%) volume changes. Crack formation is generally undesired as it aggravates the charge transport throughout the electrode or can even lead to isolation of active particles.[8] Based on the molar volumes of CuS (20.09 cm^3), Cu (7.09 cm^3), and Li_2S (28.02 cm^3), a full lithiation of CuS according to Equations (1) and (2) is accompanied by a volume expansion of 75%. This value is intermediate compared to what is expected for layered oxides and alloys. Compensation for the expansion might be obtained through free volume (voids), elastic, and plastic deformation, or by mechanisms such as crack formation. Herein, crack formation and crack evolution in SSBs are investigated by taking the CuS cathode as a model material.

As shown in **Figure 2**a and Figure S3 (Supporting Information), cracks with a strong preferential orientation perpendicular to the stack pressure direction (*z*-axis) can be observed in the electrode. The horizontal cracking is likely the result of a "z-oriented" particle expansion as suggested by Wu et al. when studying the lithiation of Sn particles.[28] The absence of observable cracks within the SE separator suggests that the cracks appearing within cathode pellets could be attributed to the volume expansion of CuS during lithiation. We could not clearly observe this oriented expansion in our cells which might be because the volume change of CuS is much smaller compared to Sn, which is known to expand to several hundred percent during lithiation. Crack formation is first observed after discharging to 1.2 V and continues to propagate during further lithiation. The preferred orientation of the cracks can be clearly seen from Figure S6 (Supporting Information), which shows the spatial distribution at the end of lithiation. The cracks remain in the electrode throughout subsequent cycling and can be observed even after 50 cycles (Figure S7, Supporting Information), i.e., the crack formation is largely irreversible. The images of the 50th cycle (charged and discharged state) appear very similar, which may indicate that the morphology of the particle and its surrounding matrix has reached a stable state. On the other hand, the capacity of the electrode decreased from 507 mAh g^{-1} to around 100 mAh g^{-1} after 50 cycles. It may therefore also be that the CuS particles become electrochemically inactive with cycling. Images of more particles, however, support that a morphologically stable state is reached over cycling, see supplementary Figure S7c,d (Supporting Information).

The tomography data were further leveraged to determine the change in crack volume during cycling (Figure 2b). In line with the images for the individual particle, cracks are absent at D1.7 V but can be detected at D1.2 V (7.6×10^6 µm^3). The crack volume increases further upon discharging reaching 9.7×10^6 µm^3 at D0.7 V. For comparison, this volume is roughly one order of magnitude larger compared to the Cu phase that forms during discharging. Charging leads to a decrease in crack volume, but around 50% of the crack volume remains at the end of charge (4.9×10^6 µm^3 at C3.0 V). Overall, the quantitative analysis is well in line with the analysis of the individual particle shown in Figure 2a. This statement could be further visualized through

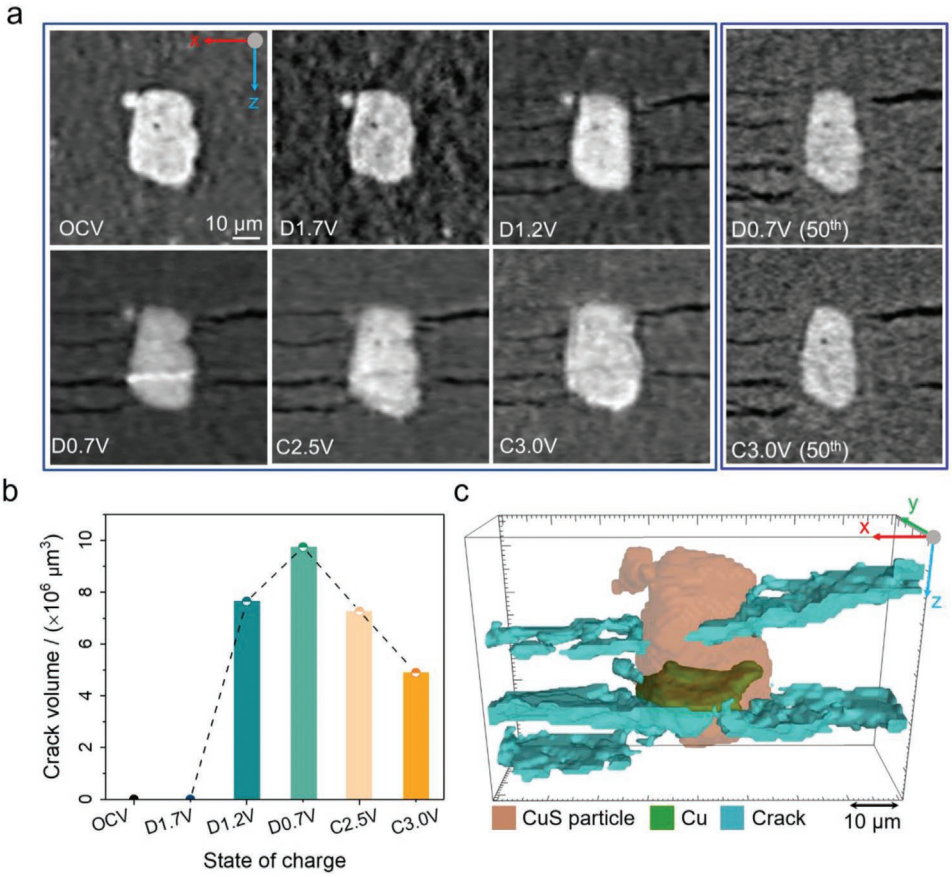

Figure 2. The formation and evolution of cracks in a CuS cathode during cycling. a) Crack evolution at different SOC during the 1st and 50th cycle. b) Quantification of the crack volume during the 1st cycle. c) A 3D rendering of the lithiated CuS particle (orange) and its surrounding cracks (cyan) together with the Cu inclusion (green) within the particle.

the dynamic structural evolution of the crack width and position, as shown in Figure S8 (Supporting Information). Meanwhile, structural changes and phase transformations lead to clear changes in the electrochemical impedance spectra during cycling (Figure S9, (Supporting Information)). Furthermore, Figure 2c gives a 3D rendering of the aforementioned features observed within and around the CuS particles, which presents the spatial distribution, orientation, and position of the CuS particle, Cu inclusion, and cracks around the particle.

2.3. z-Oriented Reversible Displacement of CAM Particles During Cycling

Active materials with large volume expansion have been widely studied in liquid electrolyte-based batteries,[29] but the degradation of SSBs due to active material volume change is still poorly understood. In light of this, we further explore the particle spatial motion in SSBs, and more importantly the concurrent and consequent microstructural degradation at the electrode-level in SSBs. Section 2.2 described crack formation resulting from the volume expansion of the CAM particles during lithiation. Volume changes, however, occur not only at the cathode but also at the anode.[30] The lithium counter electrode shrinks or expands (ideally by 100%) as lithium is consumed or plated during cycling. In fact, calculating the volume change of the complete reaction shown in Equations (1) and (2), i.e., including the volume of Li, shows that the volume of all active materials decreases by 23% during discharge. With an expanding CuS cathode and a shrinking lithium anode, one would expect a shift of the electrode particles toward the Li electrode during discharge along the *z*-axis. The process should be reversed during charging. Such a z-oriented reversible displacement can be indeed shown by the tomography data. **Figure 3**a shows the location of the CAM particles in the electrode before (OCV, left column) and after discharge (D0.7 V, middle column). In-plane (x-y plane) and cross-sectional (x-z plane) views are separately shown in the upper and lower panels. Although the CAM particles remain at roughly the same locations in the x-y plane, a clear directional displacement along the *z*-axis, i.e., toward the counter electrode is observed. This anisotropic movement can be seen from the right column where the locations of the CuS particles in the lithiated state are highlighted with yellow contours and superimposed on the images from the pristine states.

Digital volume correlation (DVC), a method used to compute the local geometric change of 3D image datasets,[31] was used to three-dimensionally probe the local volume change of the cathode. During the DVC analysis, a volume of $400 \times 400 \times 250$ μm^3 of the cathode at the pristine state was used and was further divided into five arrays each containing

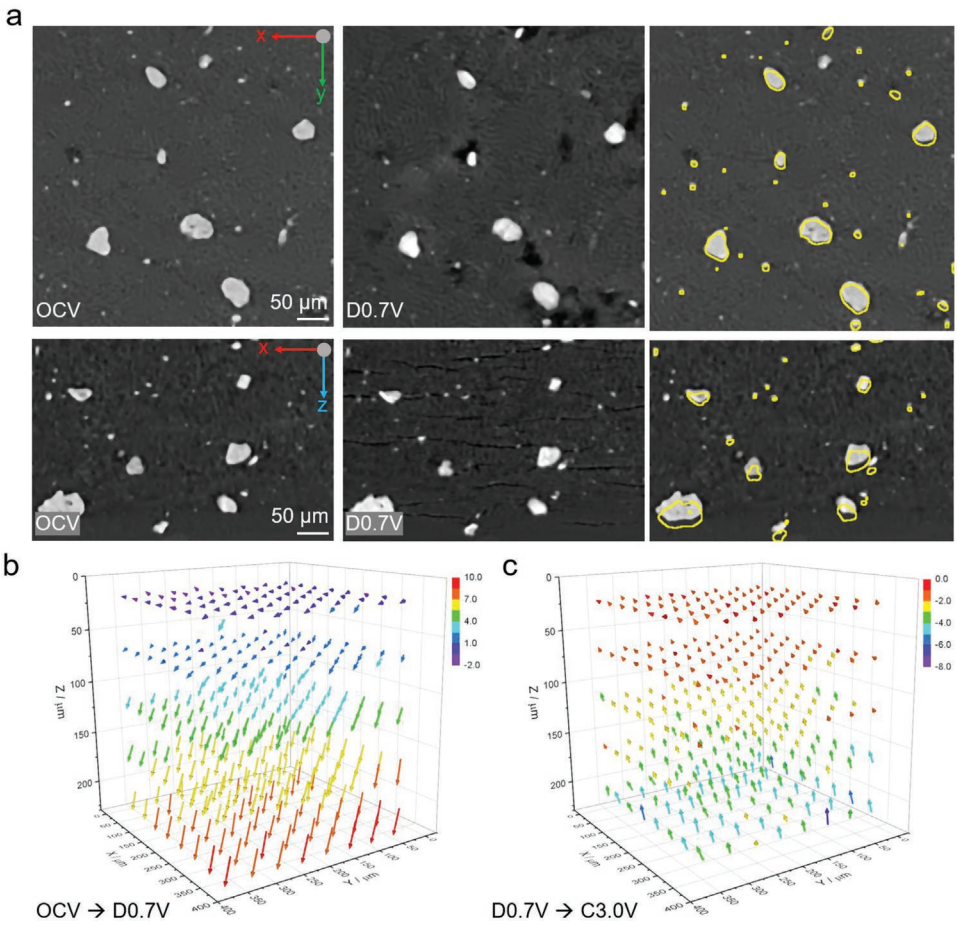

Figure 3. z-oriented reversible displacement of CAM particles during cycling a) In-plane (x-y plane) and cross-sectional views (x-z plane) of the CuS electrode before (OCV, left column) and after discharge (D0.7 V, middle column). In the right column, to visualize the spatial displacement of the CAM particles, yellow contours showing the positions of the lithiated CAM particles are superimposed on the images of the pristine states. 3D characterization of the spatial displacement of the CuS electrode during b) discharge and c) charge, using a vector field obtained from digital volume correlation (DVC). During DVC analysis, an array of cuboids ($50 \times 50 \times 50$ µm^3) was obtained from a subvolume of the CuS electrode ($400 \times 400 \times 250$ µm^3). The vectors indicate the direction and distance of the displacement of the corresponding cuboids. For ease of visibility, the vectors are color-coded based on the displacement length, and are rescaled in length by a factor of 3 for visualization.

cuboids of $50 \times 50 \times 50$ µm^3 in size, i.e., overall 320 cuboids. For each cuboid, one vector was used to indicate its direction and distance of motion. The results for all cuboids are shown in Figure 3b,c. In line with the particle displacement shown in Figure 3a, lithiation causes a shift of the particles along the *z*-axis toward the Li counter electrode. It can also be seen that the CAM particles closer to the separator tend to have a larger shift along the *z*-axis compared with particles adjacent to the current collector ($z = 0$). On average, the array closest to the SE separator shifts nearly 7.2 µm, while that closest to the current collector is usually displaced by less than 1 µm. This behavior is due to the volume changes at both electrodes that occur simultaneously, but that show opposing trends (discharging the cell leads to CAM expansion and Li shrinkage). So at least two processes need to be taken into account when considering the particle displacement during cycling. For the present case, the most dominant factor causing the particle displacement seems to be the lithium counter electrode. Assuming a planar lithium counter electrode and an ideal dissolution of Li, the discharge process would lead to a decrease in thickness of 18 µm for the Li electrode (Figure S10, Supporting Information). This value agrees well with the motion of the cathode/SE interface of 14.2 µm (Figure S10, Supporting Information). In line with these observations, the reverse process takes place during charging with a preferred displacement of the particles towards the CuS electrode, see Figure 3c.

Overall, the data reveal for the first time an anisotropic reversible displacement of CAM particles within SSBs. This phenomenon can be anticipated to widely exist in SSBs that use active materials that exhibit large volume changes during cycling, such as metals, alloys, or other conversion reactions.

2.4. Mitigating Crack Formation by Increasing Stack Pressure

The observed formation of cracks and voids during cycling of SSBs is believed to be a major cause for poor electrode utilization and capacity loss. This can be mitigated to some extent by optimizing the pellet fabrication pressure and the stack pressure (pressure during cycling),[4–6,17] but studies on how the

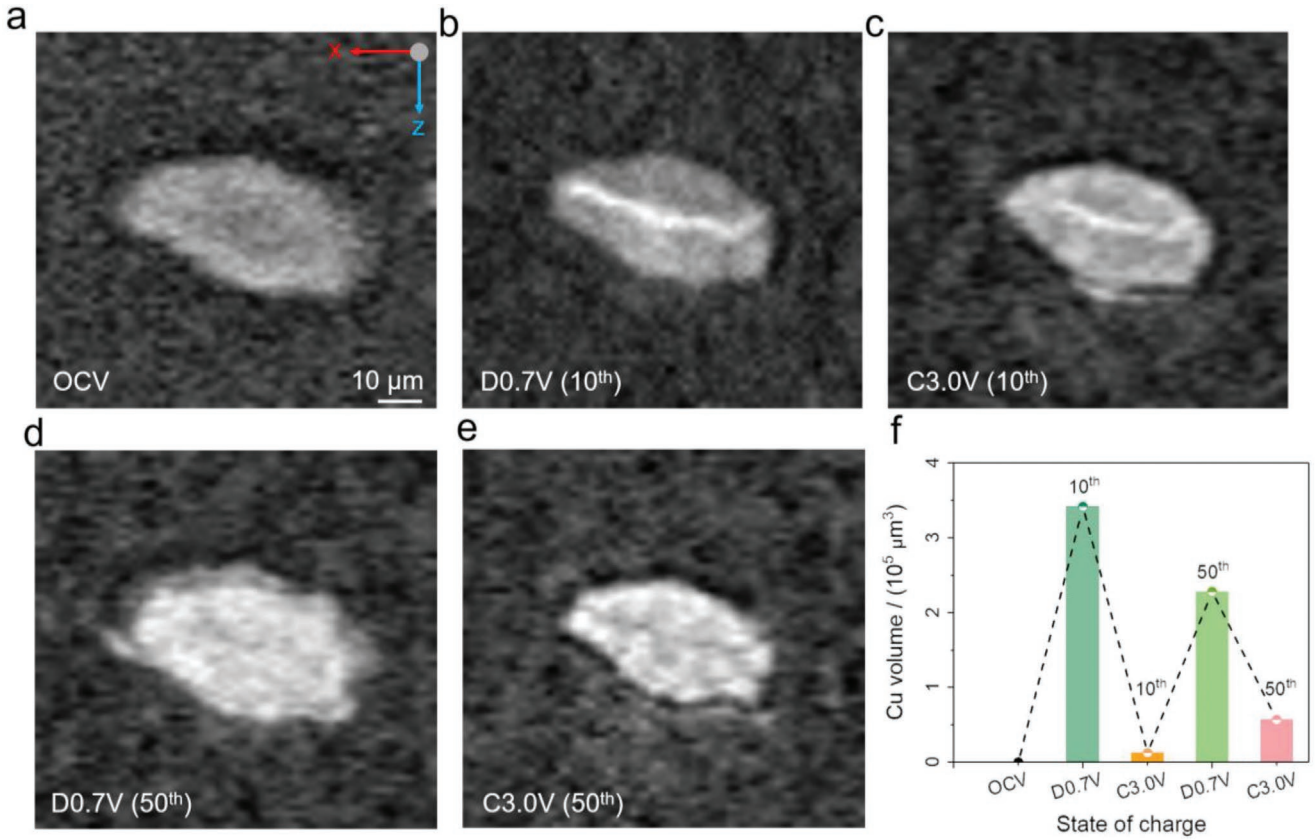

Figure 4. Microstructural evolution of SSBs under elevated stacking pressure (40 MPa). a–e) Cross-sectional view of a CuS particle at OCV and the de/lithiated states, showing the typical local phase transformation of a CuS particle during the 10th and 50th cycles. f) Volume quantification of the Cu-inclusions within the probed sub-volume of the cathode at the end of lithiation (D0.7 V) and delithiation (C3.0 V) after 10 and 50 cycles.

stack pressure impacts the inner microstructure are still scarce, especially under in situ conditions.[4,8]

The results discussed so far were obtained at a stack pressure of 26 MPa. Increasing the pressure to 40 MPa proved to be effective for eliminating nearly all cracks, as can be seen in the cross-sectional views in **Figure 4**a–e and Figure S11 (Supporting Information). At the same time, the electrode reaction still takes place in the same way, with the reversible formation of Cu inclusions during discharging/charging (see images for the 10th and 50th cycle). This is also supported by quantitative analysis (Figure 4f) showing volume changes similar to what was found at lower pressure (Figure 1e). These results collectively suggest that an increased stack pressure can effectively suppress crack formation in SSBs without impacting the phase transformation within the CAM particles.

2.5. Change of Stack Pressure During Cycling

Although pressure changes during cycling have been discussed in SSBs, this has generally been investigated with layered oxide CAMs where (de)intercalation reactions occur with relatively small volume changes.[2,30,32] It can be anticipated that electrodes composed of conversion-type materials that exhibit phase transformations, high theoretical capacities, and large volume changes during cycling could show a different behavior, but such cases have rarely been investigated. A force sensor was therefore used to continuously follow the pressure change during cycling, see Figure S12 (Supporting Information). To compare with the other results, measurements were performed by taking the low (26 MPa, denoted as L-SSB) and high (40 MPa, H-SSB) stack pressures as starting points. The voltage profiles and corresponding changes in pressure are shown in the top and bottom panels of **Figure 5**, respectively. Both cells delivered comparable capacities during discharge with 571 mAh g^{-1} for the L-SSB and 598 mAh g^{-1} for the H-SSB.

The pressure change over time is nonlinear and seems strongly influenced by the electrode reaction, which is different from the more gradual pressure changes of SSBs composed of layered oxides and alloys such as Li/NCM-811,[2] (Sb/ Sn/ Si)/ NCM-111,[30] and In/LCO.[32] The largest pressure changes were found directly after assembly where the cells were equilibrated for 24 h (rest period, black line). The pressure decreased by 4.0 MPa (–15.5%) for the L-SSB and by 3.6 MPa (–9.0%) for the H-SSB. This relaxation is caused by further densification of the SSB through particle rearrangement or plastic/elastic deformation which minimizes the remaining porosity leading to a mechanically more stable state.[33,34]

Additional but smaller pressure changes occur when discharging/charging the cells. From the onset of discharge (blue line), the stack pressures decrease which is in line with the expectation because, as mentioned above, the total volume of

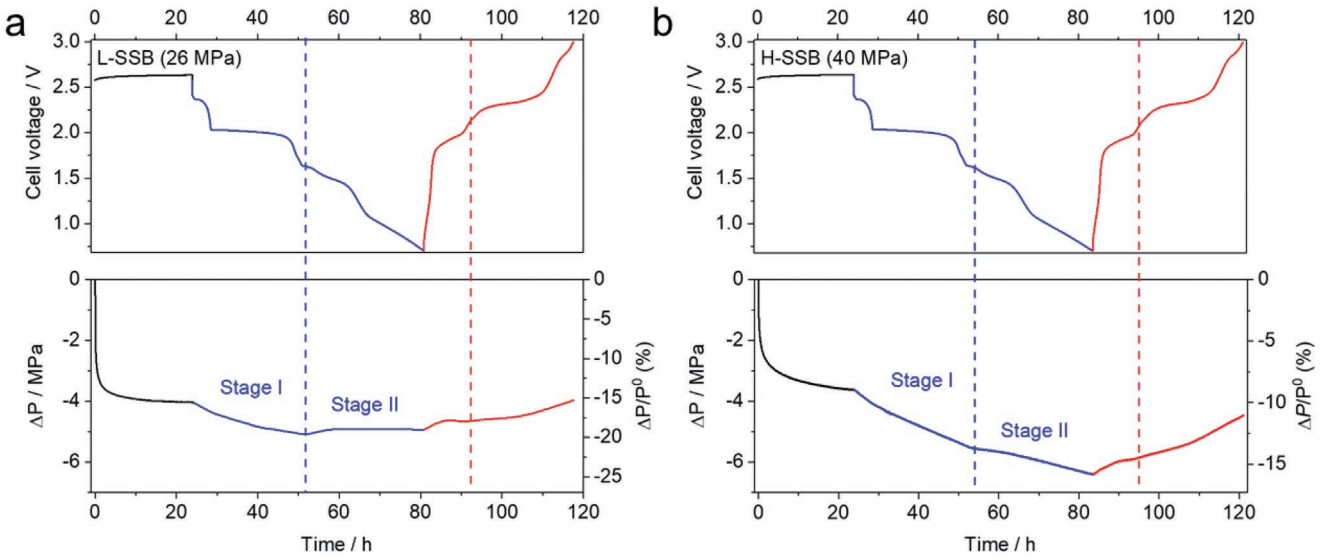

Figure 5. Change in stack pressure during cycling. Voltage profiles (top) and change in stack pressure (bottom) of Li|β-Li_3PS_4|CuS SSBs under an initial stack pressure of a) 26 MPa and b) 40 MPa at 50 mA g^{-1}. The profiles during rest, discharge, and charge periods are separately plotted in black, blue, and red, respectively. P° corresponds to the initial stack pressure, ΔP refers to the difference between the measured pressure and the initial stack pressure.

active materials decreases during discharging (–23%). The trend is reversed during charging for which an increase in pressure (ΔP becomes less negative) is found for both cells. An important observation is that the slope of ΔP suddenly changes when a step in the voltage profile occurs. The discharge curves can therefore be separated into two stages, which are visually separated by the blue dashed lines in Figure 5a,b. The sudden change in the voltage profile is the result of the two-step reaction mechanism ($CuS \rightarrow Cu_2S \rightarrow Cu$, see Equations (1) and (2)) which is found to have a direct impact on the pressure change. The differences in molar volumes of CuS (V_m = 20.09 cm^3 mol^{-1}), Cu_2S (V_m = 28.42 cm^3 mol^{-1}), and Cu (V_m = 7.09 cm^3 mol^{-1}) are the likely cause for this. The sudden change in the voltage profile is also visible during charging, although it is not as distinct (red dashed line), as can be observed by the smearing out of the step highlighted with the red dashed line relative to that of the discharge curve. Overall, however, the pressure change can be taken as a second predictive method for following the reaction process.

While the overall trend in the change in pressure is similar for both cells, clear differences can be observed during stages 1 and 2 of the discharge that necessitate further discussion. In the case of H-SSB, the pressure continuously decreases during both stages. In contrast, the stage 2 process in L-SSB is characterized by a relatively stable pressure (even a small pressure increase can be seen). This difference can be rationalized by the concomitant dissolution of Li anode and the crack evolution in the CuS cathode during discharge. For L-SSB, the continuous decrease of the stack pressure could potentially be attributed to the dissolution of the Li anode during stage 1, but being followed by a subsequent compensation by the evolving cracks that appear after the first plateau (during stage 2, i.e., after D1.7 V, Figure 2). This can lead to the observation of a roughly stable pressure during stage 2. In contrast, the absence of µm-level cracks in the cathode of H-SSB brings about a continuous pressure decrease over both stage 1 and 2. Overall, monitoring the pressure during cycling provides additional information on the cell reaction and sudden phase changes can be readily identified. Note that the in situ cell required CAM content of only 8 wt%. For practical cells with higher CAM, one would expect much more drastic changes. The discharge curves show a kink around 2.3 V which could result from side reactions of the SE with the carbon additive (Figure S13, Supporting Information).

3. Discussion

Recently, employing Li|SE|Li symmetric cells, several in situ/operando studies using XRT have promoted our understanding of the Li/SE interphase evolution,[11,12] SE cracking,[10,13,35] and short-circuiting[6] in SSBs. However, the knowledge on the interrelation between the cell chemistry, the microstructure and the mechanical properties is still poor, especially when electrode reactions with large capacities and volume expansion are applied. CuS is a CAM that turns out to be very well suited for XRT measurements. This is because the reaction with lithium leads to phases with very different attenuation coefficients and because Cu forms as µm-sized crystals thanks to a unique displacement mechanism. Because of this, the phase transformations can be well studied by XRT and the microstructural evolution can be determined. This section contains a discussion of the most important findings of this study while also mentioning some limitations that complicate a generalized mechanism up to this point.

It is important to realize that the reversibility of the displacement reaction and physical motion of the CuS particles in SSBs is observed despite the large volume changes during cycling.[18] To alleviate the volume change induced microstructure instability and deterioration within SSBs, the ductility of the cell components is crucial. For the SSBs studied here, most compounds can be considered as ductile materials (Note S1,

Supporting Information).[36] The Pugh ratio decreases for the materials of interest according to Cu_2S (4.04) > Li (2.8) > CuS (2.79) > Cu (2.54) > β-Li_3PS_4 (1.93), i.e., all materials, especially the Cu_2S intermediate phase from which Cu forms, are ductile. Only Li_2S (1.21) shows a Pugh ratio that is below the ductility threshold of 1.75.[37] It is reasonable to assume that the high ductility of the cell components is a major advantage for the realization of SSBs based on electrode materials with large volume expansion. A similar situation seems more challenging for Sn or Si anode electrodes which form more brittle Zintl phases form with Li. Modeling would be an important tool for gaining greater insight into the chemo-mechanical interplay between the components of interest during cell cycling. This approach, however, is still in its infancy due to its extreme complexity.[38–40]

Apart from the ability to follow the reaction by in situ tomography, an important finding is that discharging leads to the formation of Cu inclusions and cracks with preferred orientation in the x-y plane, i.e., perpendicular to the stack pressure (*z*-axis). The preferred orientation of the cracks can be explained by a "z-oriented" electrode expansion[28] which is because expansion along the *z*-axis is easier as compared to the x-y plane where the cell dimensions are fixed by the cell housing. This leads to the formation of cracks perpendicular to the *z*-axis following the Irwin modified Griffith's fracture mechanics, i.e., via a plastic zone existing at the tip of the cracks.[41] Recent work by Sakka et al. demonstrated that contact loss and void are more easily form at the CAM and SE interfaces in the planes perpendicular to the stack pressure direction after battery fabrication.[42] Such a phenomenon may occur in this study and facilitate the propagation of cracks in the x-y plane in SSBs. The preferred orientation of the cracks roughly along the x-y plane is particularly problematic, as these cracks intersect with the diffusion path of the charge carriers (Li^+ and e^-) in the cell, potentially limiting rate performance.

For active materials that undergo volume changes during redox reactions in SSBs, local stress/strain tends to accumulate alongside the volume expansion of the active materials. At sites where the strain/stress is high, cracks tend to develop and propagate with lithiation.[43–47] This could be more severe when materials that exhibit large volume changes are employed, such as alloy-based anodes, sulfur cathode, etc.[48] Nevertheless, crack formation may not always occur, as it can be mitigated by increasing the stack pressure as we demonstrate in this work. Strategies such as adopting cathode and anode materials with volume changes that are able to compensate for one another, or taking advantage of novel electrode architectures that are specifically designed to be robust and accommodate local stress/strain fields are potential solutions for suppressing crack formation.

An exact understanding of the formation mechanism of the Cu inclusions remains beyond the scope of this study. However, some reasonable arguments can be made. From Figure 2a, it is evident that crack formation occurs before Cu precipitation under a stack pressure of 26 MPa. These cracks, along with other defects such as grain boundaries and voids are likely sites for the heterogeneous nucleation of Cu during discharge.[49] The cracks/voids at the CAM/SE interface provide free volume and lower strain, which could make these locations the preferred sites for extruding the Cu phase from the CAM lattice. This also helps explain why the Cu phase forms within the parent CAM particles rather than around them.[24] Under higher stack pressure, the formation of µm-level cracks can be mitigated (Figure 4) though, but nm-level voids can still exist to facilitate the nucleation of Cu. The Cu inclusion that is observable in SSBs under low and high stack pressure as well as in liquid cells[24] suggests that the origin of the Cu inclusions could be attributed to the nature of the particle (e.g., grain boundaries and voids within the particle that are too small to be detected by XRT).

Our results also show that increasing the stack pressure is effective in mitigating crack formation. The absence of µm-level cracks facilitates the migration of electrons and ions, and thus leads to a remarkable increase of the initial coulombic efficiency from 32% to 70% when increasing the pressure from 26 to 40 MPa. However, the improved pressure only has a moderate impact on the overall capacity and cycle life (Figure S14, Supporting Information). Higher pressures generally lead to better electrochemical performance arising from improved physical contact between the particles,[50] but this effect might not be rate determining at the applied current density (50 mA g^{-1}) in this study. The discharge capacities at the elevated stack pressure (40 MPa) are slightly higher than those of the battery at 26 MPa over almost all 50 cycles (Figure S14, Supporting Information). Although the µm-level cracks can be suppressed under high stack pressure, thereby facilitating the migration of electrons and ions, the high current-induced polarization may play a dominant role, especially in SSBs. This impacts the dis/charge capacities, and thus only leads to a slightly improved performance under high stack pressure conditions at high current density. At the same time, higher pressures may also cause problems because plastic deformation of the lithium electrode can lead to short-circuiting.[14] Therefore, we emphasize that further systematic testing is necessary in order to obtain a more general picture on the impact of crack formation on overall cell performance.

4. Conclusion

In situ X-ray tomography was used to investigate the electrode reaction and its related microstructural evolution for a CuS CAM in Li-SSBs. The formation and dissolution of µm-sized Cu inclusions within the CAMs could be clearly followed during cycling. An important finding is that these Cu inclusions show a strong preferential orientation within the x-y plane of the cell, i.e., perpendicular to the applied pressure axis. When lithiating CuS, the formation of µm-sized Cu inclusions is preceded by the formation of observable cracks starting from 1.2 V which show a similar preferential orientation. The cracks propagate horizontally along the x-y plane, which is likely caused by a z-oriented expansion of the electrode. Charging leads to a partial recovery of the cracks. Crack formation could be effectively suppressed by increasing the stack pressure from 26 to 40 MPa. However, crack suppression was not determined to have a significant impact on the capacity or cycle life. Using DVC, the tomography data also revealed for the first time a z-oriented reversible displacement of up to 14.2 µm of the cathode/SE

interface during cycling of the SSB. This displacement is due to the plating/stripping of the Li counter electrode and can be expected to occur in all Li-SSBs. The displacement of the CAM is largest for the particles closest to the separator and smallest for the particles closest to the current collector. Operando pressure measurements showed that the reaction can also be followed with a force sensor. Sudden changes in the voltage profile result in sudden changes in the stack pressure. The study provides the most complete picture to date of the reaction of a CuS CAM in Li-SSBs and illustrates how the combination of electrochemical measurements, tomography, and pressure measurements can promote a comprehensive understanding of the reaction mechanism and microstructural evolution in SSBs.

5. Experimental Section

Materials: CuS was purchased from Thermo Fisher (Kandel) GmbH (200 mesh, 99.8%). β-Li_3PS_4 was received from BASF. Super C65 conductive carbon black was purchased from Imerys Graphite & Carbon. Li was received from Rockwood (120 µm thickness; 99.8%). All reagents were obtained from commercial suppliers and used as received without further purification unless otherwise specified.

Assembly of Solid-State Batteries: The SSBs were assembled in a homemade two-electrode PEEK battery frame with 6 mm diameter space for loading materials along with 6 mm diameter stainless steel pistons. The CuS, β-Li_3PS_4, and C65 were hand-ground in weight ratios of 8:87:5 for 15 min. For making the SSBs, a bilayer pellet composed of 25 mg β-Li_3PS_4 and 14.4 mg cathode was pelletized by applying a uniaxial pressure of 375 MPa for 3 min, and then 2 layers of Li (diameter: 4.5 mm; thickness: 120 µm) were attached to the anode side of the electrolyte. An initial stacking pressure of 26 or 40 MPa was then applied to the SSBs, which was controlled by a torque wrench. Since the β-Li_3PS_4 is moisture sensitive, all batteries were made in an Ar-filled glovebox (MBraun) with well-controlled oxygen and water concentrations lower than 1.0 ppm.

Synchrotron X-Ray Tomography Characterization: All the X-ray tomograms except that of the pristine state of the SSBs under 40 MPa stack pressure were acquired at the BAMline end-station at the BESSY II electron storage ring of the Helmholtz-Zentrum Berlin, Germany. The beam was monochromatized to 35 keV using a double multilayer monochromator that provided an energy resolution of about $\Delta E/E \approx 4\%$. The beam was directed onto the sample and the transmitted and refracted X-rays were converted to visible light using a 60 µm thick $CdWO_4$ scintillator. Images were collected using a PCO4000 camera with a 4008 × 2672 pixel CCD sensor with 10 times magnification. To increase the density resolution, a 2 × 2 camera binning was applied, leading to a pixel size of ≈0.88 µm and a field of view of 3.4 (width) × 2.3 (height) mm^2. For each tomogram, 2256 projections and 170 flatfields with an exposure time of 0.7 s for each projection/flatfield were taken over a 180° sample rotation. The obtained raw image datasets were normalized using darkfields and flatfields before being reconstructed via filtered back projection using the reconstruction codes developed at the beamline based on the tomopy Python package.[51]

The tomography of the pristine state of the SSBs under 40 MPa stack pressure was carried out at the P05 beamline at DESY. Similarly, a monochromatic X-ray beam (40 keV) was used and directed onto the SSBs with the transmitted X-rays converted to visible light by a scintillator ($CdWO_4$, 100 µm thick). An optical lens system (5×) and a Ximea CB500MG camera system were used, generating a field of view of (7.29 × 5.52) mm^2 with a nominal pixel size of 0.92 µm. A total of 4001 projections were recorded over a rotation of 180° with an exposure time of 0.05 s for each projection. The obtained raw image datasets were normalized, filtered, and reconstructed using the ASTRA Toolbox written in MATLAB.[52,53] After image reconstruction, pixel classification and image segmentation were performed with ilastik software.[54] The following datasets, alignment, and quantification analysis of the acquired 3D datasets were conducted using Fiji software. 2D and 3D image rendering were made using Avizo or VGSTUDIO MAX 3.1.

Electrochemical Characterization: The SSBs with low stacking pressure were examined at open-circuit voltage (OCV), during discharge at 1.7 V (D1.7 V), 1.2 V (D1.2 V), and 0.7 V (D0.7 V), and during charge at 2.5 V (C2.5 V) and 3.0 V (C3.0 V). The electrochemical states were controlled using a BioLogic SP-150 under the given current densities which were calculated based on the beamtime schedule. The SSBs were then cycled constantly at 50 mA g^{-1} for 50 cycles using a BioLogic BCS 805. The high stacking pressure SSB was first cycled at 10 mA g^{-1} for the 1st cycle, and then the current was increased to 50 mA g^{-1} for another 50 cycles with a BioLogic BCS 805. All SSBs were cycled in the voltage range from 0.7 to 3.0 V versus Li^+/Li. All cell capacities were calculated based on the mass of CuS.

FIB-SEM and EDX Characterization: A Zeiss Crossbeam 340 dual beam FIB-SEM with an EDX detector was used to characterize the CAM particles at pristine and lithiated states. The composite CuS was transferred using a dedicated sample transfer box from a glovebox to the FIB-SEM. FIB cutting and milling were performed at room temperature with a gallium ion beam at 30 kV. Typically, 3 nA was used for cutting and a smaller current (700 pA) for fine milling. After the CuS particles were partially cut away by FIB, an electron beam of 15 kV was used for imaging and EDX elemental mapping.

XRD Characterization: XRD profiles of the received CuS, β-Li_3PS_4, and the prepared cathode were recorded with a D2 Phaser X-ray diffractometer from Bruker. A Cu K_α X-ray tube (30 kV, 10 mA) was used and measurements were taken over an angular range of 10–70° (2θ) with a step size of 0.02°.

Operando Pressure Measurements: The change in battery pressure during cycling was recorded in a homemade operando setup. A K-450 compressive force sensor from Lorenz Messtechnik GmbH allows for force measurements in the range of 1–10 kN with 0.1% accuracy. The sensor is calibrated with standard reference weights before testing. The pressure evolution of the SSBs was then tested at 25 °C, which was held constant inside a BINDER MK-56 oven. The SSBs were fabricated using the same procedure as that for tomography measurements, but with the addition of a force sensor at the bottom of the SSBs. The stack pressure was then manually controlled until reaching 26 or 40 MPa.

Supporting Information

Supporting Information is available from the Wiley Online Library or from the author.

Acknowledgements

Z.G.Z. thanks the China Scholarship Council (CSC) for funding. P.A. acknowledges support from the projects NASEBER (No. 03XP0187D) and KAROFEST (No. 03XP0498A) funded by the Bundesministerium für Bildung und Forschung (BMBF). The authors acknowledge BESSY II for the beamtime allocation at the BAMline end-station and thank Michael Sintschuk for the support during the experiments. They also acknowledge DESY (Hamburg, Germany), a member of the Helmholtz Association HGF, for the provision of experimental facilities. Parts of this research were carried out at P05 beamline. The authors thank Helmholtz-Zentrum Berlin for the FIB-SEM measurement time allocation (CoreLab CCMS) and Holger Kropf for technical assistance. They also acknowledge Thermo Fisher Scientific for providing Avizo and the XDigitalVolumeCorrelation Extension for software evaluation as well as technical support during evaluation.

Open access funding enabled and organized by Projekt DEAL.

Conflict of Interest

The authors declare no conflict of interest.

Author Contributions

Z.Z. and K.D. contributed equally to this work. P.A., I.M., Z.G.Z., and K.D. conceived the study. Z.G.Z. assembled the batteries and performed the electrochemical measurements. K.D. carried out the X-ray tomography measurements and conduct the data analysis. A.H. assisted the tomography data analysis. H.M. and F.W. supported the tomography experiments. K.D. performed FIB-SEM and EDX characterization. Z.G.Z. and T.H. designed and built the operando pressure measuring instrument. Z.G.Z., K.D., K.A.M., I.M., and P.A. interpreted the data. I.M. and P.A. supervised the research. The manuscript was written by Z.G.Z., K.D., K.M., and P.A. with input and review from all the other coauthors.

Data Availability Statement

The data that support the findings of this study are available from the corresponding author upon reasonable request.

Keywords

copper sulfide, crack evolution, digital volume correlation, phase transformation, solid-state batteries, stack pressure evolution, X-ray tomography

Received: September 15, 2022
Revised: October 28, 2022
Published online:

[1] J. Janek, W. G. Zeier, *Nat. Energy* **2016**, *1*, 16141.
[2] R. Koerver, W. Zhang, L. De Biasi, S. Schweidler, A. O. Kondrakov, S. Kolling, T. Brezesinski, P. Hartmann, W. G. Zeier, J. Janek, *Energy Environ. Sci.* **2018**, *11*, 2142.
[3] M. Yamamoto, Y. Terauchi, A. Sakuda, A. Kato, M. Takahashi, *J. Power Sources* **2020**, *473*, 228595.
[4] T. Shi, Y.-Q. Zhang, Q. Tu, Y. Wang, M. C. Scott, G. Ceder, *J. Mater. Chem. A* **2020**, *8*, 17399.
[5] J.-M. Doux, Y. Yang, D. H. S. Tan, H. Nguyen, E. A. Wu, X. Wang, A. Banerjee, Y. S. Meng, *J. Mater. Chem. A* **2020**, *8*, 5049.
[6] J. M. Doux, H. Nguyen, D. H. S. Tan, A. Banerjee, X. Wang, E. A. Wu, C. Jo, H. Yang, Y. S. Meng, *Adv. Energy Mater.* **2020**, *10*, 1903253.
[7] A. Banerjee, X. Wang, C. Fang, E. A. Wu, Y. S. Meng, *Chem. Rev.* **2020**, *120*, 6878.
[8] R. Koerver, I. Aygün, T. Leichtweiß, C. Dietrich, W. Zhang, J. O. Binder, P. Hartmann, W. G. Zeier, J. Janek, *Chem. Mater.* **2017**, *29*, 5574.
[9] F. Sun, K. Dong, M. Osenberg, A. Hilger, S. Risse, Y. Lu, P. H. Kamm, M. Klaus, H. Markötter, F. García-Moreno, T. Arlt, I. Manke, *J. Mater. Chem. A* **2018**, *6*, 22489.
[10] Z. Ning, D. S. Jolly, G. Li, R. De Meyere, S. D. Pu, Y. Chen, J. Kasemchainan, J. Ihli, C. Gong, B. Liu, D. L. R. Melvin, A. Bonnin, O. Magdysyuk, P. Adamson, G. O. Hartley, C. W. Monroe, T. J. Marrow, P. G. Bruce, *Nat. Mater.* **2021**, *20*, 1121.
[11] J. A. Lewis, F. J. Q. Cortes, Y. Liu, J. C. Miers, A. Verma, B. S. Vishnugopi, J. Tippens, D. Prakash, T. S. Marchese, S. Y. Han, C. Lee, P. P. Shetty, H.-W. Lee, P. Shevchenko, F. De Carlo, C. Saldana, P. P. Mukherjee, M. T. McDowell, *Nat. Mater.* **2021**, *20*, 503.
[12] F. Sun, C. Wang, M. Osenberg, K. Dong, S. Zhang, C. Yang, Y. Wang, A. Hilger, J. Zhang, S. Dong, H. Markötter, I. Manke, G. Cui, *Adv. Energy Mater.* **2022**, *12*, 2103714.
[13] J. Tippens, J. C. Miers, A. Afshar, J. A. Lewis, F. J. Q. Cortes, H. Qiao, T. S. Marchese, C. V. Di Leo, C. Saldana, M. T. Mcdowell, *ACS Energy Lett.* **2019**, *4*, 1475.
[14] J. M. Doux, H. Nguyen, D. H. S. Tan, A. Banerjee, X. Wang, E. A. Wu, C. Jo, H. Yang, Y. S. Meng, *Adv. Energy Mater.* **2019**, *10*, 1903253.
[15] S. Randau, D. A. Weber, O. Kötz, R. Koerver, P. Braun, A. Weber, E. Ivers-Tiffée, T. Adermann, J. R. Kulisch, W. G. Zeier, F. H. Richter, J. Janek, *Nat. Energy* **2020**, *5*, 259.
[16] A. O. Kondrakov, A. Schmidt, J. Xu, H. Geßwein, R. Mönig, P. Hartmann, H. Sommer, T. Brezesinski, J. Janek, *J. Phys. Chem. C* **2017**, *121*, 3286.
[17] P. Minnmann, F. Strauss, A. Bielefeld, R. Ruess, P. Adelhelm, S. Burkhardt, S. R. L. Dreyer, E. Trevisanello, H. Ehrenberg, T. Brezesinski, F. H. Richter, J. Janek, *Adv. Energy Mater.* **2022**, *12*, 2201425.
[18] A. L. Santhosha, N. Nazer, R. Koerver, S. Randau, F. H. Richter, D. A. Weber, J. Kulisch, T. Adermann, J. Janek, P. Adelhelm, *Adv. Energy Mater.* **2020**, *10*, 2002394.
[19] J. Cabana, L. Monconduit, D. Larcher, M. R Palacín, *Adv. Mater.* **2010**, *22*, E170.
[20] F. Klein, B. Jache, A. Bhide, P. Adelhelm, *Phys. Chem. Chem. Phys.* **2013**, *15*, 15876.
[21] A. Débart, L. Dupont, R. Patrice, J.-M. Tarascon, *Solid State Sci.* **2006**, *8*, 640.
[22] B. Jache, B. Mogwitz, F. Klein, P. Adelhelm, *J. Power Sources* **2014**, *247*, 703.
[23] D. J. Chakrabarti, D. E. Laughlin, *Bull. Alloy Phase Diagrams* **1983**, *4*, 254.
[24] M. T. Mcdowell, Z. Lu, K. J. Koski, J. H. Yu, G. Zheng, Y. Cui, *Nano Lett.* **2015**, *15*, 1264.
[25] H.-J. Noh, S. Youn, C. S. Yoon, Y.-K. Sun, *J. Power Sources* **2013**, *233*, 121.
[26] S. Ohno, R. Koerver, G. Dewald, C. Rosenbach, P. Titscher, D. Steckermeier, A. Kwade, J. Janek, W. G. Zeier, *Chem. Mater.* **2019**, *31*, 2930.
[27] L. Y. Beaulieu, K. W. Eberman, R. L. Turner, L. J. Krause, J. R. Dahn, *Electrochem. Solid-State Lett.* **2001**, *4*, A137.
[28] X. Wu, J. Billaud, I. Jerjen, F. Marone, Y. Ishihara, M. Adachi, Y. Adachi, C. Villevieille, Y. Kato, *Adv. Energy Mater.* **2019**, *9*, 1901547.
[29] L. Zhou, K. Zhang, Z. Hu, Z. Tao, L. Mai, Y.-M. Kang, S.-L. Chou, J. Chen, *Adv. Energy Mater.* **2018**, *8*, 1701415.
[30] S. Y. Han, C. Lee, J. A. Lewis, D. Yeh, Y. Liu, H.-W. Lee, M. T. McDowell, *Joule* **2021**, *5*, 2450.
[31] K. Dong, F. Sun, A. Hilger, P. H. Kamm, M. Osenberg, F. García-Moreno, I. Manke, *J. Energy Chem.* **2023**, *76*, 429.
[32] W. Zhang, D. Schröder, T. Arlt, I. Manke, R. Koerver, R. Pinedo, D. A. Weber, J. Sann, W. G. Zeier, J. Janek, *J. Mater. Chem. A* **2017**, *5*, 9929.
[33] A. Masias, N. Felten, R. Garcia-Mendez, J. Wolfenstine, J. Sakamoto, *J. Mater. Sci.* **2019**, *54*, 2585.
[34] W. S. Lepage, Y. Chen, E. Kazyak, K.-H. Chen, A. J. Sanchez, A. Poli, E. M. Arruda, M. D. Thouless, N. P. Dasgupta, *J. Electrochem. Soc.* **2019**, *166*, A89.
[35] M. B. Dixit, N. Singh, J. P. Horwath, P. D. Shevchenko, M. Jones, E. A. Stach, T. S. Arthur, K. B. Hatzell, *Matter* **2020**, *3*, 2138.
[36] G. R. Irwin, *J. Appl. Mech.* **1957**, *24*, 361.
[37] S. Pugh, *J. Sci.* **1954**, *45*, 823.
[38] D. Bistri, A. Afshar, C. V. Di Leo, *Meccanica* **2021**, *56*, 1523.
[39] A. Bielefeld, D. A. Weber, J. Janek, *J. Phys. Chem. C* **2019**, *123*, 1626.
[40] S. Sun, C.-Z. Zhao, H. Yuan, Y. Lu, J.-K. Hu, J.-Q. Huang, Q. Zhang, *Mater. Futures* **2022**, *1*, 012101.
[41] W. D. Callister, D. G. Rethwisch, *Materials Science and Engineering*, 8th ed. (Eds: W. D. Callister, D. G. Rethwisch), Wiley, Hoboken, NJ, **2011**.
[42] Y. Sakka, H. Yamashige, A. Watanabe, A. Takeuchi, M. Uesugi, K. Uesugi, Y. Orikasa, *J. Mater. Chem. A* **2022**, *10*, 16602.
[43] T. Zhang, J. Jiang, B A. Shollock, T. B Britton, F. P. E. Dunne, *Mater. Sci. Eng., A* **2015**, *641*, 328.
[44] W. D. Musinski, D. L. Mcdowell, *Int. J. Fatigue* **2012**, *37*, 41.

[45] S. V. Suknev, M. D. Novopashin, *Dokl. Phys.* **2000**, *45.7*, 339.
[46] F. Yang, M. Tane, J. P. Lin, Y. H. Song, H. Nakajima, *Mater. Des.* **2013**, *49*, 755.
[47] L. Porz, T. Swamy, B. W. Sheldon, D. Rettenwander, T. Frömling, H. L. Thaman, S. Berendts, R. Uecker, W. C. Carter, Y. M. Chiang, *Adv. Energy Mater.* **2017**, *7*, 1701003.
[48] M. So, G. Inoue, R. Hirate, K. Nunoshita, S. Ishikawa, Y. Tsuge, *J. Electrochem. Soc.* **2021**, *168*, 030538.
[49] N. T. K. Thanh, N. Maclean, S. Mahiddine, *Chem. Rev.* **2014**, *114*, 7610.
[50] T. Krauskopf, B. Mogwitz, C. Rosenbach, W. G. Zeier, J. Janek, *Adv. Energy Mater.* **2019**, *9*, 1902568.
[51] D. A. Gürsoy, F. De Carlo, X. Xiao, C. Jacobsen, *J. Synchrotron. Radiat.* **2014**, *21*, 1188.
[52] J. Moosmann, A. Ershov, V. Weinhardt, T. Baumbach, M. S. Prasad, C. Labonne, X. Xiao, J. Kashef, R. Hofmann, *Nat. Protoc.* **2014**, *9*, 294.
[53] W. Van Aarle, W. J. Palenstijn, J. Cant, E. Janssens, F. Bleichrodt, A. Dabravolski, J. De Beenhouwer, K. J. Batenburg, J. Sijbers, *Opt. Express* **2016**, *24*, 25129.
[54] S. Berg, D. Kutra, T. Kroeger, C. N. Straehle, B. X. Kausler, C. Haubold, M. Schiegg, J. Ales, T. Beier, M. Rudy, K. Eren, J. I. Cervantes, B. Xu, F. Beuttenmueller, A. Wolny, C. Zhang, U. Koethe, F. A. Hamprecht, A. Kreshuk, *Nat. Methods* **2019**, *16*, 1226.